REPORT DOCUMENTATION PAGE

Form Approved
OMB No. 0704-0188

1. REPORT DATE *(DD-MM-YYYY)*
15-06-2010

REPRINT

4. TITLE AND SUBTITLE
V arc interplanetary coronal mass ejections observed with the Solar Mass Ejection Imager

5a. CONTRACT NUMBER

5b. GRANT NUMBER

5c. PROGRAM ELEMENT NUMBER
62601F

6. AUTHOR(S)
Kahler, S.W. and D.F. Webb*

5d. PROJECT NUMBER
5021

5e. TASK NUMBER
RD

5f. WORK UNIT NUMBER
A1

7. PERFORMING ORGANIZATION NAME(S) AND ADDRESS(ES)
Air Force Research Laboratory/RVBXS
29 Randolph Road
Hanscom AFB MA 01731-3010

8. PERFORMING ORGANIZATION REPORT NUMBER
AFRL-RV-HA-TR-2010-1051

9. SPONSORING / MONITORING AGENCY NAME(S) AND ADDRESS(ES)

10. SPONSOR/MONITOR'S ACRONYM(S)
AFRL/RVBXS

11. SPONSOR/MONITOR'S REPORT NUMBER(S)

12. DISTRIBUTION / AVAILABILITY STATEMENT
Approved for Public Release; Distribution Unlimited.

*Institute for Scientific Research, Boston College, Chestnut Hill, MA

13. SUPPLEMENTARY NOTES
REPRINTED FROM: J. GEOPHYSICAL RESEARCH, Vol 112, A09103,2007 doi: 10.1029/2007JA012358

14. ABSTRACT
Since February 2003, The Solar Mass Ejection Imager (SMEI) has been observing interplanetary coronal mass ejections (ICMEs) at solar elongation angles ϵ > 20 degrees. The ICMEs generally appear as loops or arcs in the sky, but five show distinct outward concave shapes that we call V arcs. We expect to observe some V arcs, formed by trailing edges of ICME flux ropes or by leading ICME edges sheared by solar wind (SW) speed gradients at the heliospheric current sheet. We characterize the properties of these V arcs and compare them with average properties of all SMEI ICMEs. The typical V arc speeds argue against a slow MHD shock interpretation for their structures. We estimate the V arc solar source locations and their opening angle dynamics as tests for SW shearing. The first test contradicts but the second supports the SW shearing explanation. The implications of the small number of V arcs observed with SMEI is considered. The point P approximation used to determine the V arc locations and inferred solar source regions is critically examined in Appendix A.

15. SUBJECT TERMS
Magnetic flux ropes
Coronal mass ejections Solar physics Heliospheric imaging CMEs

16. SECURITY CLASSIFICATION OF:			17. LIMITATION OF ABSTRACT	18. NUMBER OF PAGES	19a. NAME OF RESPONSIBLE PERSON
a. REPORT	b. ABSTRACT	c. THIS PAGE	SAR	9	Janet C. Johnston
UNCLAS					19b. TELEPHONE NUMBER *(include area code)* 781-377-2138

JOURNAL OF GEOPHYSICAL RESEARCH, VOL. 112, A09103, doi:10.1029/2007JA012358, 2007

V arc interplanetary coronal mass ejections observed with the Solar Mass Ejection Imager

S. W. Kahler[1] and D. F. Webb[2]

Received 21 February 2007; revised 18 April 2007; accepted 30 April 2007; published 8 September 2007.

[1] Since February 2003, the Solar Mass Ejection Imager (SMEI) has been observing interplanetary coronal mass ejections (ICMEs) at solar elongation angles $\epsilon > 20°$. The ICMEs generally appear as loops or arcs in the sky, but five show distinct outward concave shapes that we call V arcs. We expect to observe some V arcs, formed by trailing edges of ICME flux ropes or by leading ICME edges sheared by solar wind (SW) speed gradients at the heliospheric current sheet. We characterize the properties of these V arcs and compare them with average properties of all SMEI ICMEs. The typical V arc speeds argue against a slow MHD shock interpretation for their structures. We estimate the V arc solar source locations and their opening angle dynamics as tests for SW shearing. The first test contradicts but the second supports the SW shearing explanation. The implications of the small number of V arcs observed with SMEI is considered. The point P approximation used to determine the V arc locations and inferred solar source regions is critically examined in Appendix A.

Citation: Kahler, S. W., and D. F. Webb (2007), V arc interplanetary coronal mass ejections observed with the Solar Mass Ejection Imager, *J. Geophys. Res.*, *112*, A09103, doi:10.1029/2007JA012358.

1. Introduction

[2] The Solar Mass Ejection Imager (SMEI) was launched into Earth orbit on 6 January 2003 to map the sky in white light once every 102-min orbit. The goal of the SMEI mission [*Jackson et al.*, 2004] is to demonstrate the feasibility of detecting interplanetary coronal mass ejections (ICMEs) against the much brighter background sky. This is done by producing difference maps of the Thomson-scattered sunlight from density enhancements in the solar wind (SW), corrected for scattered light and sky background, to look for ICMEs as antisunward propagating features [*Webb et al.*, 2006]. The inferred ICME trajectories are essential to improve the predictions of geomagnetic storms and space weather effects [*Howard et al.*, 2006].

[3] A list of 139 ICMEs detected by SMEI through July 2004 and a discussion of their properties were given by *Webb et al.* [2006]. The primary morphology descriptors assigned to the ICMEs were: arc, blob, and loop. Those shapes were expected based on coronagraph CME images, which are nearly always characterized by convex outward leading edges. Four of the SMEI ICMEs were concave outward structures, described henceforth as V arcs, and are shown in Figure 1, along with a fifth V arc found in an extended survey of SMEI data through September 2005. Here we will characterize the properties of these few V arc ICMEs and consider three explanations for their formation, which are shown schematically in Figure 2.

[4] *Webb et al.* [2006] discussed the V arc ICMEs in terms of disconnected magnetic fields surrounding CMEs. In this view [*Webb and Cliver*, 1995], CME loops lying predominately in the plane of the sky undergo magnetic reconnection behind the CME cavity to produce the concave-outward V arcs seen in many coronagraph observations. An early survey of CMEs observed in the Large Angle and Spectrometric Coronagraph Experiment (LASCO) reported that concave-outward features were observed in at least 36% of all CMEs [*St. Cyr et al.*, 2000]. Such reconnection may well occur to produce observable vertical current sheets far behind the main CME [*Webb et al.*, 2003; *Bemporad et al.*, 2006], but the accepted interpretation of the V arc in coronagraph images [*Dere et al.*, 1999; *Chen et al.*, 2000; *Cremades and Bothmer*, 2004; *Wang and Sheeley*, 2006; *Krall*, 2007] is that it is the sunward side of a three-dimensional helical flux rope viewed along the rope axis. The flux rope is formed on emergence, before the rope center reaches 1.5 R$\odot$ [*Dere et al.*, 1999]. The cartoon of Figure 2 shows the enhanced density, which may also involve filament material, as region A on the sunward side of a flux-rope CME. The axial flux rope is one candidate interpretation of the V arcs.

[5] A second interpretation of V arcs is based on the latitudinal gradient in SW speeds detected by spacecraft during the relatively stable conditions of solar minima [*Richardson and Paularena*, 1997]. The observed gradient supports the view that low-speed ($\leq$400 km s^{-1}) SW flows outward along the heliospheric current sheet (HCS), and the speeds gradually increase to ~600 km s^{-1} at high heliomagnetic latitudes [*Odstrcil et al.*, 2004] corresponding to

[1]Space Vehicles Directorate, Air Force Research Laboratory, Hanscom Air Force Base, Massachusetts, USA.
[2]Institute for Scientific Research, Boston College, Chestnut Hill, Massachusetts, USA.

0148-0227/07/2007JA012358$09.00

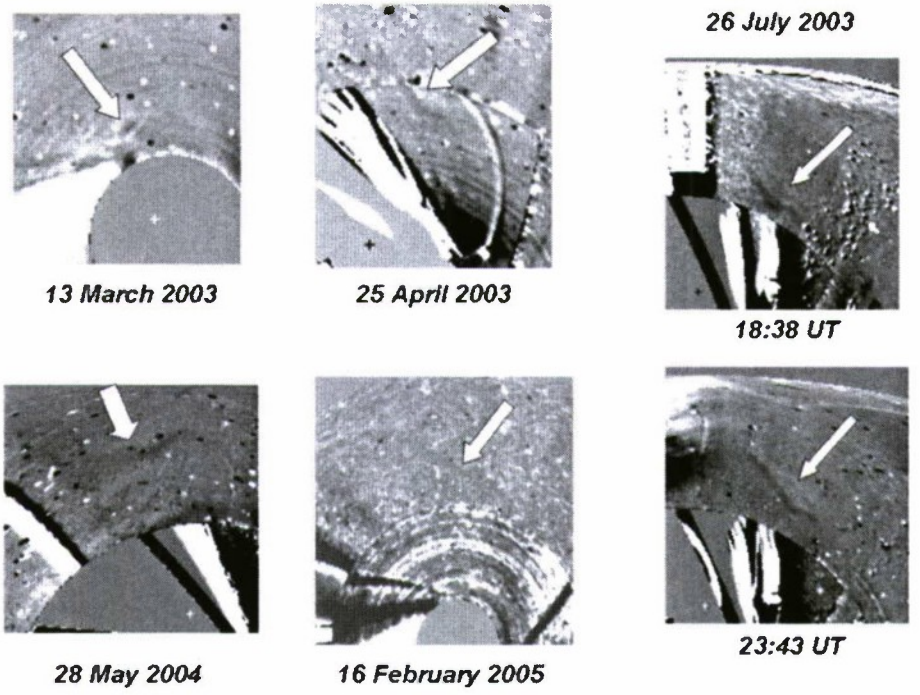

Figure 1. Orbital difference images of the five V arc interplanetary coronal mass ejections (ICMEs) of the study. The plus symbol in each image is Sun center, and the exclusion zone circle is 20° in radius. Arrows indicate positions of the V arcs. Antisunward motion of the 26 July 2003 V arc is evident in the pair of images separated by almost 5 hours in the two images on the right.

coronal hole outflows. Interplanetary scintillation observations of CME-driven shocks have shown that their propagation speeds are lower near the HCS than at other regions [*Tokumaru et al.*, 2000]. Recent work by *Liu et al.* [2006] to determine the global structure of observed magnetic clouds (MCs) based on minimum-variance analysis and the Grad-Shafranov technique [*Hu and Sonnerup*, 2002] has shown that MCs near solar maximum are very flattened and convex outward with radii of curvature proportional to their heliospheric distances. However, those MCs observed near solar minimum and propagating near the HCS were found to be concave outward with radii of curvature of ~0.3 AU.

[6] Models in which hydrodynamic CMEs [*Odstrcil et al.*, 2004] or MCs [*Owens*, 2006] are injected into the HCS show the expected ICME distortions to a concave-outward V arc morphology by the SW speed gradient. Earlier model calculations with CME injections offset from the HCS also show that the ICME is sheared into asymmetric V arc morphologies by the fast-slow SW speed gradients [*Smith et al.*, 1998; *Odstrcil and Pizzo*, 1999; *Schmidt and Cargill*, 2001]. Synthetic white light images [*Lugaz et al.*, 2005] of ICMEs modeled with more realistic simulations of injections of magnetic flux ropes into current sheets [*Manchester et al.*, 2004] clearly show the V arc morphology in meridional planes orthogonal to the HCS. The SW-sheared ICME, shown schematically as region B in Figure 2, is the second interpretation of the V arcs.

[7] The third interpretation is that of a slow MHD shock. The observation that most CME speeds are faster than the coronal sound speed but slower than the Alfven speed implies that slow MHD shocks may form ahead of some CMEs [*Hundhausen*, 1999]. Contrary to the fronts of the familiar convex-outward fast-mode MHD shocks, behind which field lines are compressed, the slow-mode MHD shocks must have concave-outward fronts to allow field line divergence, as shown in Figure 2. Numerical simulations also showed that CMEs moving slightly faster than the Alfven speed produced intermediate MHD shocks with concave-outward fronts [*Steinolfson*, 1992]. Density enhancements are produced at both kinds of the concave-outward shock fronts, and *Hundhausen* [1999] showed two concave-outward CME candidates for slow/intermediate wave fronts observed with the Solar Maximum Mission (SMM) Coronagraph/Polarimeter experiment. Images from the Large Angle Spectrometric Coronagraph (LASCO) may not have been examined for such events. Whether such shock fronts could continue to propagate outward through SW with an increasing flow speed and declining Alfven speed into the SMEI field of view is not clear. We indicate the density enhancements of these concave-outward shock fronts, the third candidate interpretation of the V arcs, as region C in Figure 2.

2. Data Analysis

2.1. V Arc ICME Characteristics

[8] The characteristics of the 139 ICMEs observed during the first 1.5 years of SMEI operation have been reviewed by *Webb et al.* [2006]. The four V arc ICMEs of that study and the more recent one found in observations through September 2005 are listed in Table 1. For each ICME we give the date of observation, the position angle (PA) and compass

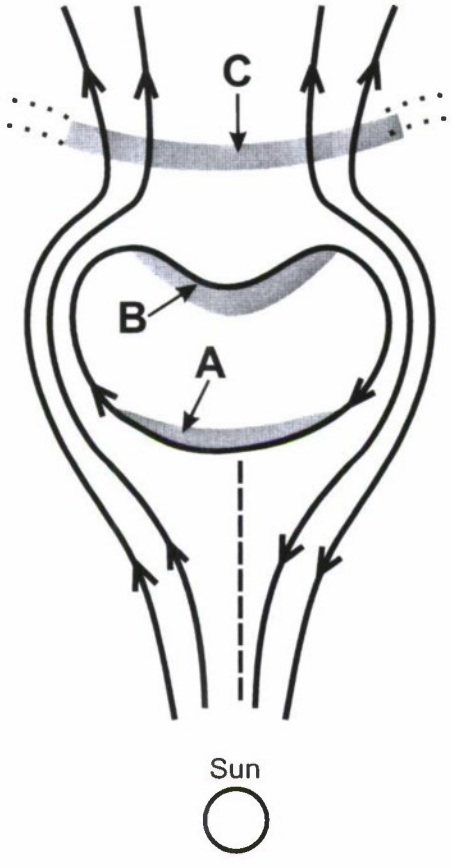

Figure 2. Meridional plane schematic of the three candidates for V arcs. Shading indicates density enhancement regions composing the V arcs and solid lines are magnetic field lines. The single closed line indicates the outer boundary of a magnetic flux rope. A is the location of dense material, perhaps a cool filament, on the sunward side of the flux rope overlying a current sheet (dashed line). B is compressed material at the leading edge of the flux rope distorted into a concave-outward geometry by latitudinal gradients in SW speed. C is material compressed at a slow or intermediate MHD shock behind which the fields diverge or change latitudinal directions, respectively. A and C might be expected to occur close to the Sun, but B is gradually formed in the interplanetary medium by the accumulated SW speed shear.

direction, the angular span W, and the observed range of the elongation angle from the Sun ϵ. The mean values of the characteristics of the 139 SMEI ICMEs given in Table 2 of *Webb et al.* [2006] serve as the basis for a comparison of the five V arc ICMEs with the full population. The V arc ICMEs are typical in durations (12–50 hours versus mean 16 hours), W (20°–50° versus average 42°), and angular speeds (0.6–1.54°/hour versus mean 1.1°/hour). The midranges of ϵ are somewhat larger for the V arc ICMEs (23°–83° versus 36° median), where we have determined the median midrange ϵ from Table I of *Webb et al.* [2006]. The PAs of all five V arcs were north of the ecliptic plane. *Webb et al.* [2006] did not discuss the distribution of their ICME PAs, but when we assign compass directions to the ICMEs of their Table 1, we find 97 ICME PAs north and only 41 south of the ecliptic plane. If the V arcs are typical ICMEs, the formal probability that all five V arcs would lie north of the ecliptic plane is $(97/138)^5 = 0.17$. The northern V arc PAs are therefore not inconsistent with this imbalance for all the ICMEs, which is mainly due to a loss of southern sky coverage during South Atlantic Anomaly passages of SMEI. Within our limited statistics the V arc ICMEs are not distinguished from other ICMEs in any way other than by morphology.

[9] With the V arc PAs and ϵ-time profiles extrapolated back to the Sun we can look for associated solar flares and CMEs. We found a probable solar flare association for only one of the V arcs and give its size and location in Column 6 of Table 1; flare associations were not found (NF) for the other ICMEs. Some information in Table 1 of *Webb et al.* [2006] on the V arc of 26 July 2003 was based on an incorrect ϵ-time plot; corrected values are given in our Table 1. Columns 7 through 12 give the start times, PAs and Ws, and speeds of associated CMEs observed in LASCO and reported in either the Catholic University catalog [*Yashiro et al.*, 2004] or the CACTus (Computer Aided CME Tracking) catalog [*Robbrecht and Berghmans*, 2004; *Robbrecht et al.*, 2006]. Connecting an ICME to an associated flare or LASCO CME must be accomplished across a broad gap in time and elongation angle [*Webb et al.*, 2006], so these associations must be considered tentative. On the basis of our extrapolated solar launch times (column 2 of Table 2), we found associated LASCO CMEs in both catalogs for the first two ICMEs, as did *Webb et al.* [2006], and a frontside flare signature for only one. Furthermore, our LASCO CME associations for the 13 March and 25 April ICMEs are each significantly earlier than those of *Simnett* [2005]. We therefore find that only two of the five V arc ICMEs may be associated with confirmed CMEs. The numbers here are small, but these CME associations are fewer than the *Simnett* [2005] preliminary figure of $\geq$75% for the general population of SMEI ICMEs. With a time window of ±12 hours he found that only 11 of 80 SMEI ICMEs had no associated LASCO CMEs and nine others had only very faint candidates.

2.2. Testing for SW Shears on ICMEs

2.2.1. Sources of ICMEs on Synoptic Charts

[10] To determine whether the V arcs are due to SW shears on the ICMEs at the HCS we tested the V arc observations in two ways. The first test was to see whether the V arc locations lay near the projected HCSs, as expected if SW shears are the primary cause of the V arcs. We projected the inferred trajectories of the V arcs onto the Wilcox Solar Observatory Potential Field Source Surface (PFSS) synoptic charts to compare the source regions with the HCSs, as shown in the bottom of Figure 3. The "classic" charts with the PFSS located at 2.5 $R_\odot$ were used. The PFSS synoptic charts predict interplanetary magnetic field directions at 1 AU on a daily basis with an ~85% accuracy [*Zhao et al.*, 2006] and therefore should be sufficiently accurate in the inner heliosphere for determining the HCS locations.

[11] We used the point P approximation (see Appendix A) for the five V arcs at times of their first observations to

Table 1. V Arc Interplanetary Coronal Mass Ejections (ICMEs) Observed by the Solar Mass Ejection Imager (SMEI) With Large Angle and Spectrometric Coronagraph Experiment (LASCO) and Computer Aided CME Tracking (CACTus) Associations

		SMEI[a]			SOLAR	LASCO[b]			CACTus[c]		
Year	Date	PA[d]	Span W	ϵ Range	Solar Flare Size/Loc	Start Date/UT	PA/W	Speed, km/s	Start Date/UT	PA/W	Speed, km/s
2003	13 Mar	20°/NNE	20°	17°–29°	NF	12/0020	355°/93°	411	12/0006	357°/86°	289
	25 Apr	330°/NW	50°	26°–47°	M2.0/N20W22	23/1555	343°/105°	596	23/1650	329°/70°	328
	26 Jul	320°/NW	40°	37°–69°	NF		NF			NF	NF
2004	28 May	13°/NNE	48°	46°–72°	NF		NF			NF	
2005	16 Feb	353°/N	40°	74°–92°	NF		NF			NF	

[a]Data from *Webb et al.* [2006].
[b]From http://cdaw.gsfc.nasa.gov/CME_list/.
[c]From http://sidc.oma.be/cactus/scan/scan.html.
[d]Measured counterclockwise from north. SMEI position angles (PAs) in solar ecliptic coordinates. LASCO and CACTus PAs in solar heliographic coordinates.

determine their radial projections onto the solar disk. The SMEI image maps are produced only in sidereal and solar ecliptic coordinates [*Webb et al.*, 2006], so transformations to solar heliographic coordinates are necessary to plot the projections on the PFSS synoptic charts. We transformed V arc PAs to solar heliographic coordinates and used a Sun-centered coordinate system with the north pole at the sub-Earth point. That system is convenient because ϵ is the complement of the colatitude ϕ measured from its pole (Appendix A). The V arc projections in that system were rotated into the heliographic system. Linear extrapolations from the V arc ϵ-time plots determined the approximate solar launch times of Table 2, and the projected solar longitudes were shifted westward assuming a solar rotation rate of 13.3°/day to locate the Carrington latitudes and longitudes of the solar source regions on the synoptic charts.

[12] The results are summarized in Table 2. For each V arc we give the date, estimated solar launch time, the calculated source latitude and longitude, and the angular offsets from the nearest HCS location measured in degrees directly north-south and east-west if the HCS reached the source latitude. Since we have an associated flare location for the 25 April V arc, we also include the flare source in Table 2. Note that that flare and associated LASCO CME (Table 1) occurred about 14 hours before the launch time projected from the ϵ-time plots. We show the ϵ-time plot and PFSS synoptic chart for that event in Figure 4. The launch of the CME associated with the 13 March V arc occurred only 4 hours before the projected launch used in Table 2. The point P approximation produces uncertainties of the solar source locations that we estimate to be perhaps 20°–30°. If we assume constant radial speeds and compact V arc structures, then we can use the fixed-ϕ model, discussed in Appendix A, to estimate ϕ. Our comparison of the V arc ϵ-time profile shapes with those of Appendix A indicates that the range of ϕ is 20°–60°. Note that the trajectory of the 25 April V arc (Figure 4) is slightly concave upward and a good match to the $\phi = 20°$ plot of Appendix A, which is also consistent with the W22° associated flare location. The matches furthermore indicate that for $\phi \leq 50°$ our linear extrapolations of ϵ to 0° will yield V arc launch times somewhat delayed from actual, again consistent with the 14-hour time difference between the inferred launch and the flare/CME for the 25 April V arc. Correcting for delayed launches would shift source regions a few degrees further west to higher Carrington longitudes.

[13] Despite the crude technique, the large calculated separations of the V arc sources from the HCS locations preclude the SW shear interpretation for at least the two V arcs of 25 April and 28 May. Only the 26 July V arc appears consistent with a launch close to the HCS. If we assume that a V arc can be produced when only one flank of an ICME is sheared by the SW, then their half widths, W/2, all $\leq 25°$, may allow SW shearing for the flanks of the 13 March and 16 February V arcs. In summary, however, the calculated source locations do not support the SW-shearing V arc interpretation.

2.2.2. Dynamics of V Arc Structures

[14] The second test for the SW-shearing interpretation of the V arcs is to determine whether the angular speeds $d\epsilon/dt$ of the V arc flanks exceed those of their vertices. If SW shearing is occurring during the observations, the angles formed by the V arcs should be shrinking, or converging with time. We used the near real-time difference (NRTD) image maps to measure ϵ at the transitions between the leading bright components and the trailing dark components

Table 2. Offsets of V Arc ICME Sources From the Heliospheric Current Sheet (HCS)

V Arc Date	Launch Time and Date	Carrington Latitude	Carrington Longitude	HCS Offset Directions
13 Mar	0400 UT 12 Mar	N60°	62°	N23° –
25 Apr	0600 UT 24 Apr	N43°	298°	N98° –
Flare	1600 UT 23 Apr	N20°	279°	N82° E86°
26 Jul	0600 UT 25 Jul	N42°	156°	S14° E24°
28 May	1200 UT 26 May	N43°	27°	N77° E56°
16 Feb	1600 UT 14 Feb	N09°	148°	N23° E44°

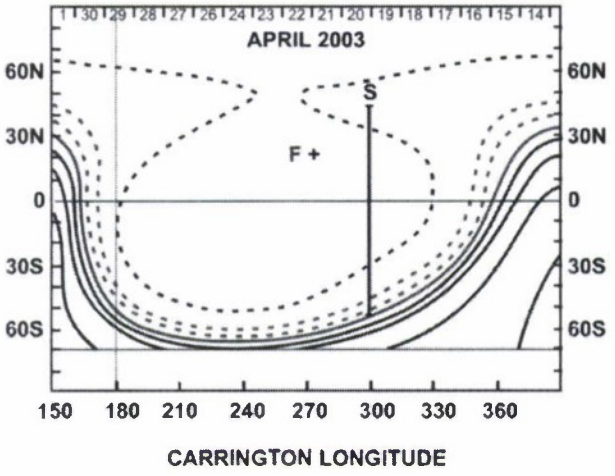

Figure 3. Locations of the calculated V arc source region S and associated solar flare F on the Carrington Potential Field Source Surface synoptic chart. The N-S displacement of source region S from the heliospheric current sheet is indicated.

[*Webb et al.*, 2006]. For each V arc we measured positions at the eastern and western edges and at the vertex. Linear least squares fits were made to determine each $d\epsilon/dt$, and those values with their PAs are given in the second through fourth columns of Table 3. The PAs of the edge locations, which were generally not sharply defined, are averages only, and for the vertices we give the range of PAs, which generally showed small drifts to higher (eastward) or lower (westward) values. The last column of Table 3 gives the dynamic configuration: converging, as expected for SW shear, or diverging, as expected for dense material in an expanding flux rope.

[15] Three of the five V arcs show clear convergence. Unfortunately, the east and west ends of the 16 February V arc were faint and difficult to measure, so the few available points gave rise to errors too large for a clear determination. Direct comparison of the vertex and wing speeds indicates a clear diverging configuration for the 25 July ICME. For three of the four V arcs the evidence favors the converging dynamics, and therefore the SW-shear interpretation, in contrast to the result in section 2.2.1, in which the ICME solar source locations constituted evidence against SW shear.

3. Discussion

[16] The five V arc ICMEs of this study are not distinguished from the general ICME population by properties other than their morphology. In particular, their speeds appear typical, so it is not obvious why these ICMEs should be slow or intermediate shocks, one of our candidate interpretations. Furthermore, the V arcs are distinctly kinked at their vertices, contrary to the gradual curvature of feature C in Figure 2. It is also not clear that density accumulations at driven slow or intermediate shocks would form features sufficiently dense to be the primary or only observable structures of ICMEs. A more general open question is whether the ICMEs observed by SMEI are sometimes or ever shock fronts. In the few cases of possible fast-mode shocks identified in LASCO CMEs the shock fronts were much fainter than the CME core structures [*Vourlidas et al.*, 2003]. Thus we conclude that the V arc slow-shock candidate labeled C in Figure 2 and discussed in section 1 is very unlikely.

[17] A morphology somewhat similar to the V arcs was observed in a LASCO Halo CME on 6 November 1997, in which the CME legs showed an unusual broad divergence with height away from the center of the CME. *Plunkett et al.* [2002] suggested that the fast (>1500 km s^{-1}) ejection material of that CME may have interacted with the ambient corona or moved into regions evacuated by earlier CMEs from the same region. Since other CMEs similar to that of 6 November have not been reported, and the two bent legs were not joined together as our V arcs are, we do not offer this suggestion as a candidate origin of the V arcs.

[18] We performed two observational tests of the SW shear interpretation of the V arcs. The comparison of the solar source sites inferred from the point P approximation found only one of the five V arcs near (<20°) an HCS location on the PFSS synoptic charts, which does not favor the SW-shear interpretation. On the other hand, the only V arc with a source near the HCS, that of 26 July, is the only V arc which shows a diverging dynamics, inconsistent with SW shearing, but perhaps consistent with an expanding flux rope geometry. If we assume that the point P methodology can be very misleading, as discussed in the Appendix, then perhaps the V arc dynamics test should be considered the more definitive test, thereby supporting the SW shearing interpretation.

[19] When CMEs are launched into the HCS, the SW-speed shears are expected to form V arc ICMEs. However, the SMEI survey of ICME morphologies, extended to 205 ICMEs observed through September 2005, has yielded only five V arc candidates. The V arc launch sites relative to the HCS on the PFSS charts, although crudely determined using

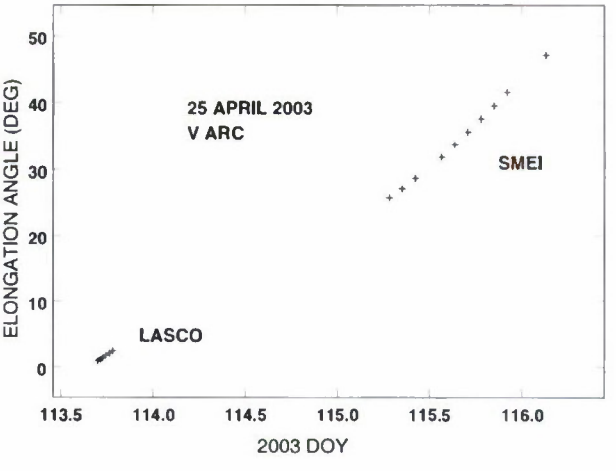

Figure 4. Plot of ϵ-time for the Solar Mass Ejection Imager (SMEI) V arc ICME of 25 April 2003 and the associated Large Angle and Spectrometric Coronagraph Experiment CME. The solar launch time projected from the SMEI plot is day of year (DOY) 114.25, about 4 hours later than the CME onset.

Table 3. Angular Elongation Speeds and PAs of V Arc ICMEs

	dϵ/dt, deg/day and PA			
V Arc Date	West	Vertex[a]	East	Type
13 Mar	18.7 ± 1.6 at 6°	14.2 ± 0.2 at 17°–24°	17.1 ± 1.0 at 35°	converging
25 Apr	26.3 ± 0.9 at 322°	22.0 ± 1.0 at 343°–340°	28.1 ± 2.8 at 357°	converging
26 Jul	26.0 ± 0.4 at 306°	31.3 ± 0.9 at 324°–319°	26.2 ± 0.7 at 345°	diverging
28 May	31.7 ± 1.1 at 2°	21.1 ± 0.5 at 19°–14°	24.6 ± 1.1 at 29°	converging
16 Feb	43.6 ± 24.7 at 340°	24.9 ± 1.4 at 354°–358°	8.9 ± 4.0 at 17°	uncertain

[a]Angular range of PA in solar ecliptic coordinates from earliest to latest measurements.

the point P model, indicated that two V ares were certainly, and two V ares were probably, launched well away from the HCS (Table 2). Only the 26 July ICME launch coordinates lay close to the HCS. This suggests that the observed ICMEs only rarely propagate through the HCS, contrary to the usual assumption [e.g., *Manchester et al.*, 2004]. Sources of CMEs observed on the SMM were predominantly confined to large-scale magnetic regions, particularly streamers [*Hundhausen*, 1993] whose latitudinal variations generally track those of the calculated HCS throughout the solar cycle. *Gopalswamy et al.* [2003] found that the latitudinal ranges of CMEs associated with filament eruptions generally tracked the tilts of the HCS. However, *Subramanian et al.* [1999] found that nearly half (46%) the LASCO CMEs overlapped streamers in coronagraph synoptic maps but did not disrupt the streamers and only 16% of all CMEs disrupted the streamers. We do not know of any comparisons of CME source regions with associated HCS locations, rather than with streamer locations, but our finding of so few V ares in the ICME population (5 of 205) appears consistent with the lack of streamer disruptions found by *Subramanian et al.* [1999] and with ICME launches displaced from the HCS.

[20] The interpretation of the V ares would benefit greatly from their observations in both the LASCO and SMEI fields of view. The large angular separation between the radial fields of view of LASCO (<8°) and SMEI (>18° and clearly evident in Figure 4) not only precludes following the development of observed CME morphologies from one instrument to another, it provides a surprising challenge simply to identify LASCO-SMEI associations for individual CMEs [*Simnett*, 2005]. This unfortunate situation will be improved when we have the overlapping coronal and heliospheric fields of view from the SECCHI instrument suite on the new STEREO mission [*Howard et al.*, 2000].

4. Conclusions

[21] The V arc ICMEs of this study are only a small fraction (~3%) of all the observed SMEI ICMEs, but they have durations, widths, and angular speeds typical of the general ICME population. The V arc speeds and kinked vertices argue against a slow-shock interpretation of their formation. We employed two observational tests to look for evidence of a V arc origin in SW shears. In the first, we found that four of the five V arc sources lay well away from the HCS on the PFSS synoptic charts. This result argues against the SW shear interpretation, but the source locations are dependent on the point P approximation, as discussed in Appendix A. The second and more definitive test showed a temporal convergence of the V arc angles in three cases, as expected for SW shear, and divergence for only one case, that being the V arc originating near the HCS. An origin in SW shear is slightly favored by these tests, but with conflicting results in a small data sample, we cannot rule out the flux rope interpretation.

Appendix A: Point P and Fixed-ϕ Distances and Speeds of ICMEs

A1. Point P Method

[22] A major challenge in tracking the trajectories of ICMEs is to determine their positions accurately in space when the SMEI observations yield only the solar position angles PA and the elongation angles ϵ of ICMEs as functions of time. The point P approximation illustrated in Figure A1 is a convenient method that provides a low-limit estimate of the ICME distance from the Sun $r(P)$ [*Howard et al.*, 2006]. The primary assumption is that the brightest part of an observed ICME is due to the columnar density along a spherical front or shell that lies along a Sun-centered sphere, shown as point P in the planar projection of Figure A1. Point P is the region of maximum Thomson scattering strength by the ICME electrons for the observer at Earth [*Vourlidas and Howard*, 2006]. This method readily yields the conversion of the observed ϵ into distance $r(P)$ from Sun center in units of AU by

$$r(P) = \sin\epsilon. \tag{A1}$$

As Figure A1 indicates, any observed feature located along the line of sight and either closer to (point B) or farther from (point A) the Earth than P must also be at a greater distance from the Sun than $r(P)$.

[24] The point P approximation has been used to determine not only ICME distances $r(P)$ but also their speeds $dr(P)/dt$ [e.g., *Howard et al.*, 2006; *Webb et al.*, 2006] from the $r(P)$ versus t plots based on the approximation. For very wide (≥100°) ICMEs the point P model may work well. However, if the brightest component or the entire ICME should be a narrow or compact structure, then a serious deficiency of the point P model is that the point P trajectory of the ICME from Sun to Earth begins near the solar limb at $\phi \sim 90°$ and follows a curved path through 90° to reach the Earth at $\phi \sim 0°$. This trajectory is called the Thomson surface by *Vourlidas and Howard* [2006] and is illustrated in their Figure 1. In addition to underestimating the distance r, the derived speeds could also be in significant error. Note that while the point P method assumes that the Earth will

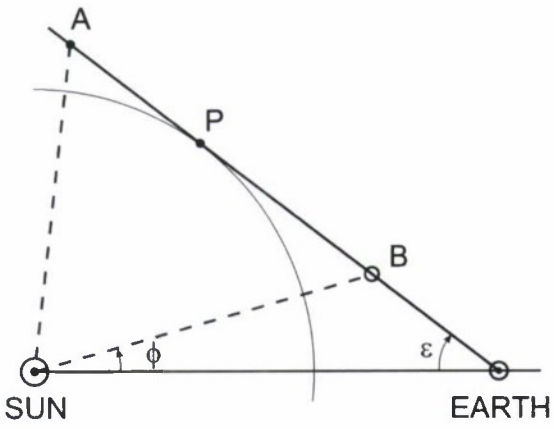

Figure A1. ICME planar geometry for the point P and fixed-ϕ models. The elongation angle of the ICME observed from SMEI at Earth is ϵ, and ϕ is the solar colatitude of the ICME measured in a coordinate system with the solar sub-Earth point as the pole. This coordinate system is convenient with the use of the SMEI ϵ measurements. In the point P approximation the ICME distance from the Sun r is derived by assuming that the ICME front is always tangent to the Sun-centered circle. Compact ICMEs located at A or B will be at solar distances r (dashed lines) greater than those inferred from the point P method; thus the point P method provides a lower limit to r. A similar schematic is shown in Figure 1 of *Howard et al.* [2006].

necessarily intercept the ICME, that method alone can not determine whether an ICME is Earth-directed, a crucial factor for space weather forecasting.

A2. Fixed-ϕ Method

[25] Another approach to the ICME location is to assume that the ICME is a relatively compact structure moving radially away from the Sun. From Figure A1 we find that for radial motion from a source at colatitude ϕ this fixed-ϕ method gives the distance from Sun center in units of AU as

$$r(\phi, \epsilon) = \tan\epsilon \times [\sin\phi + \tan\epsilon \cos\phi]^{-1}. \quad \text{(A2)}$$

[26] The relationship between ϵ and the distance $r(\phi)$ is shown in Figure A2 for radial trajectories with fixed ϕ. ICMEs moving antisunward at uniform speeds will produce tracks similar to those in the figure, which may be a useful diagnostic for ϕ. However, $r(\phi)$ can be determined from SMEI observations only with supplemental information on the ICME location such as (1) the solar source location derived from associated flare observations, (2) the line-of-sight distance of the ICME from the plane of the sky derived from measurements of polarized brightness [*Moran and Davila*, 2004; *Dere et al.*, 2005], (3) the separately determined Doppler line-of-sight and plane-of-sky speeds [*Ciaravella et al.*, 2006] or (4) the variation of the brightness with $r(\phi)$ for an assumed fixed ICME mass calculated by *Vourlidas and Howard* [2006]. By assuming a uniform ICME speed and mass with the fixed-ϕ model, we can use Figure 3 of *Vourlidas and Howard* [2006] and our Figure A2

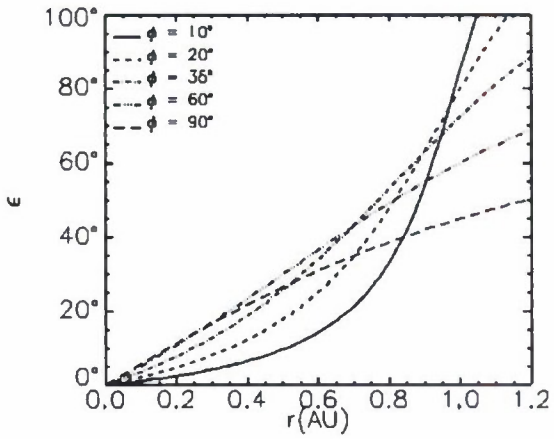

Figure A2. Elongation angle ϵ observed at Earth versus the Sun-ICME distance r for several values of the colatitude ϕ defined in Figure A1. Compact ICMEs moving uniformly antisunward would trace such trajectories in ϵ-time plots.

for at least a qualitative assessment of ϕ. Near-limb ($\phi > 60°$) ICMEs will increase nearly linearly in ϵ with time but decline rapidly in brightness with ϵ, while nearly Earth-directed ($\phi < 35°$) ICMEs will increase faster than linearly in ϵ with time but decline only slowly in brightness with ϵ.

A3. Comparisons of Positions and Speeds for the Methods

[27] Figure A3 shows the ratio of $r(P)$ to $r(\phi)$ as a function of ϵ for several values of ϕ. The agreement is optimum (worst) when P lies near (far from) the solar source fixed-ϕ. For most colatitudes and a SMEI observing range of $\sim 20° < \epsilon < \sim 80°$ [*Webb et al.*, 2006], $r(P)$ is underestimated relative to $r(\phi)$ by no more than ~20%. Larger underestimates are incurred for ICMEs when ϵ and ϕ are both large or both small.

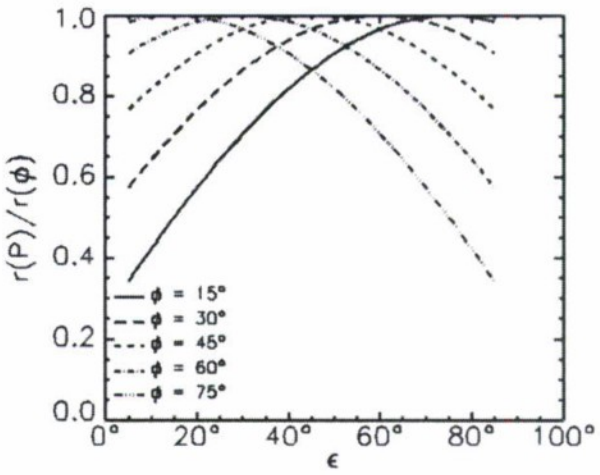

Figure A3. Ratios of inferred ICME distances $r(P)/r(\phi)$ as a function of elongation angle ϵ, plotted for solar colatitude values of ϕ = 15°, 30°, 45°, 60°, and 75°.

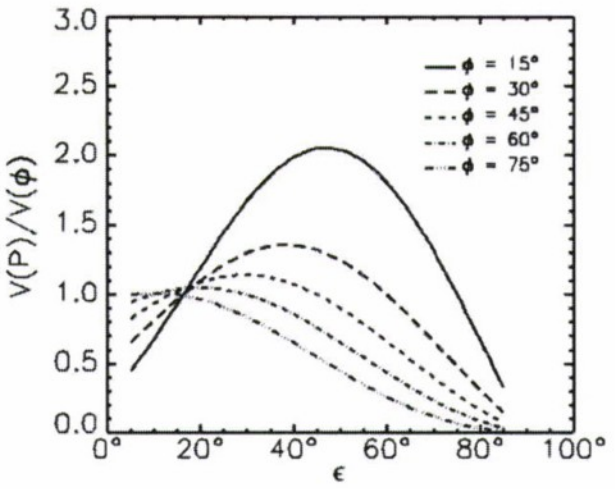

Figure A4. Ratios of inferred speeds $V(P)/V(\phi)$, plotted as a function of ϵ.

[28] Less obvious is the divergence between the two models in terms of their inferred ICME speeds. Again, we can compare the two models by taking the differentials of equation (A1):

$$dr(P) = \cos\epsilon d\epsilon. \tag{A3}$$

and equation (A2):

$$dr(\phi) = \left[Q^{-1}\sec^2\epsilon - Q^{-2}\tan\epsilon\cos\phi\sec^2\epsilon\right]d\epsilon \tag{A4}$$

where $Q = \sin\phi + \tan\epsilon\cos\phi$.

[29] The ratio of the point P speed $V(P) = dr(P)/d\epsilon$ to the fixed-ϕ speed, $V(\phi) = dr(\phi)/d\epsilon$, as a function of ϵ is shown in Figure A4 for the same five values of colatitude ϕ shown in Figure A3. Again taking $V(\phi)$ as the standard, we see that the inferred $V(P)$ is in good agreement at the small (<30°) ϵ range, can be higher or lower by a factor of 2 at intermediate (40°–60°) ϵ, and can be much smaller at large (>70°) ϵ. The assertion of *Webb et al.* [2006] that the point P approximation gives a reasonable approximation to the true speeds of ICMEs viewed by SMEI must be considered in this light. However, appropriate CME and ICME geometries are a focus of continuing work [e.g., *Morrill et al.*, 2006]. A series of recent CME models [*Xue et al.*, 2005; *Michalek*, 2006] is based on a cone geometry, in which a spherical front overlays a cone projecting from the Sun. The angular width of the cone then is the important parameter to determine whether the point P or the fixed-ϕ model is more appropriate. Matching the models to loop-arcade or flux-rope geometries suggested by some observations [*Cremades and Bothmer*, 2004; *Dere et al.*, 2005] may require the arcade or flux-rope orientations in space for optimum modeling.

[30] The point P and fixed-ϕ speed differences also imply possible significant errors or uncertainties in ICME accelerations derived from SMEI observations. For example, a compact ICME with a uniform radial speed and well described by the fixed-ϕ model may appear first to accelerate and then to decelerate ($\phi < 50°$) or to decelerate continuously from the Sun to 1 AU ($\phi > 60°$) when described in the point P model. Thus not only the magnitude but also the sign of the acceleration can be in error. These ICME accelerations are crucial for predicting space weather effects and for modeling the drag or acceleration forces [*Tappin et al.*, 2004; *Tappin*, 2006; *Howard et al.*, 2006].

[31] **Acknowledgments.** SMEI is a collaborative project of the U.S. Air Force Research Laboratory, NASA, the University of California at San Diego, the University of Birmingham, U.K., Boston College, and Boston University. Financial support has been provided by the U.S. Air Force, the University of Birmingham, and NASA. D.F.W. acknowledges support from AFRL contracts AF19628-00-C-0073 and FA8718-06-C-0015 and NASA grant NNG05GF98G. The LASCO CME catalog is generated and maintained at the CDAW Data Center by NASA and the Catholic University of America in cooperation with the Naval Research Laboratory. SOHO is a project of international cooperation between ESA and NASA. Wilcox Solar Observatory data used in this study were obtained via the web site http://wso.stanford.edu courtesy of J.T. Hoeksema. The Wilcox Solar Observatory is currently supported by NASA. We thank the reviewers for their helpful comments.

[32] Zuyin Pu thanks Kenneth P. Dere and Jeff Morrill for their assistance in evaluating this paper.

References

Bemporad, A., G. Poletto, S. T. Suess, Y.-K. Ko, N. A. Schwadron, H. A. Elliott, and J. C. Raymond (2006), Current sheet evolution in the aftermath of a CME event, *Astrophys. J., 638*, 1110–1128.

Chen, J., R. A. Santoro, J. Krall, R. A. Howard, R. Duffin, J. D. Moses, G. E. Brueckner, J. A. Darnell, and J. T. Burkepile (2000), Magnetic geometry and dynamics of the fast coronal mass ejection of 1997 September 9, *Astrophys. J., 533*, 481–500.

Ciaravella, A., J. C. Raymond, and S. W. Kahler (2006), Ultraviolet properties of halo coronal mass ejections: Doppler shifts, angles, shocks, and bulk morphology, *Astrophys. J., 652*, 774–792.

Cremades, H., and V. Bothmer (2004), On the three-dimensional configuration of coronal mass ejections, *Astron. Astrophys., 422*, 307–322.

Dere, K. P., G. E. Brueckner, R. A. Howard, D. J. Michels, and J. P. Delaboudiniere (1999), LASCO and EIT observations of helical structure in coronal mass ejections, *Astrophys. J., 516*, 465–474.

Dere, K. P., D. Wang, and R. Howard (2005), Three-dimensional structure of coronal mass ejections from LASCO polarization measurements, *Astrophys. J., 620*, L119–L122.

Gopalswamy, N., A. Lara, S. Yashiro, and R. A. Howard (2003), Coronal mass ejections and solar polarity reversal, *Astrophys. J., 598*, L63–L66.

Howard, R. A., J. D. Moses, and D. G. Socker (2000), Sun-Earth connection coronal and heliospheric investigation (SECCHI), in *Instrumentation for UV/EUV Astronomy and Solar Missions*, edited by S. Fineschi et al., *Proc. SPIE, 4139*, 259–283.

Howard, T. A., D. F. Webb, S. J. Tappin, D. R. Mizuno, and J. C. Johnston (2006), Tracking halo coronal mass ejections from 0–1 AU and space weather forecasting using the Solar Mass Ejection Imager (SMEI), *J. Geophys. Res., 111*, A04105, doi:10.1029/2005JA011349.

Hu, Q., and B. U. O. Sonnerup (2002), Reconstruction of magnetic clouds in the solar wind: Orientations and configurations, *J. Geophys. Res., 107*(A7), 1142, doi:10.1029/2001JA000293.

Hundhausen, A. J. (1993), Sizes and locations of coronal mass ejections: SMM observations from 1980 and 1984–1989, *J. Geophys. Res., 98*(A8), 13,177–13,200.

Hundhausen, A. (1999), Coronal mass ejections, in *The Many Faces of the Sun*, edited by K. T. Strong et al., pp. 143–200, Springer-Verlag, New York.

Jackson, B. V., et al. (2004), The solar mass ejection imager (SMEI) mission, *Sol. Phys., 225*, 177–207.

Krall, J. (2007), Are all coronal mass ejections hollow flux ropes?, *Astrophys. J., 657*, 559–566.

Liu, Y., J. D. Richardson, J. W. Belcher, C. Wang, Q. Hu, and J. C. Kasper (2006), Constraints on the global structure of magnetic clouds: Transverse size and curvature, *J. Geophys. Res., 111*, A12S03, doi:10.1029/2006JA011890.

Lugaz, N., W. B. Manchester IV, and T. I. Gombosi (2005), The evolution of coronal mass ejection density structures, *Astrophys. J., 627*, 1019–1030.

Manchester, W. B., IV, T. I. Gombosi, I. Roussev, A. Ridley, D. L. De Zeeuw, I. V. Sokolov, K. G. Powell, and G. Toth (2004), Modeling a space weather event from the Sun to the Earth: CME generation and

interplanetary propagation, *J. Geophys. Res.*, *109*, A02107, doi:10.1029/2003JA010150.
Michalek, G. (2006), An asymmetric cone model for halo coronal mass ejections, *Solar Phys.*, *237*, 101–118.
Moran, T. G., and J. M. Davila (2004), Three-dimensional polarimetric imaging of coronal mass ejections, *Science*, *305*, 66–70.
Morrill, J. S., R. Howard, and D. Webb (2006), Impacts of viewing geometry on CME observations in the heliosphere, *Bull. Am. Astron. Soc.*, *38*, 231.
Odstrcil, D., and V. J. Pizzo (1999), Distortion of the interplanetary magnetic field by three-dimensional propagation of coronal mass ejections in a structured wind, *J. Geophys. Res.*, *104*(A12), 28,225–28,239.
Odstrcil, D., P. Riley, and X. P. Zhao (2004), Numerical simulation of the 12 May 1997 interplanetary CME event, *J. Geophys. Res.*, *109*, A02116, doi:10.1029/2003JA010135.
Owens, M. J. (2006), Magnetic cloud distortion resulting from propagation through a structured solar wind: Models and observations, *J. Geophys. Res.*, *111*, A12109, doi:10.1029/2006JA011903.
Plunkett, S. P., D. J. Michels, R. A. Howard, G. E. Brueckner, O. C. St. Cyr, B. J. Thompson, G. M. Simnett, R. Schwenn, and P. Lamy (2002), New insights on the onsets of coronal mass ejections from SOHO, *Adv. Space Res.*, *29*(10), 1473–1488.
Richardson, J. D., and K. I. Paularena (1997), Streamer belt structure at solar minima, *Geophys. Res. Lett.*, *24*, 1435–1438.
Rohbrecht, E., and D. Berghmans (2004), Automated recognition of coronal mass ejections (CMEs) in near-real-time data, *Astron. Astrophys.*, *425*, 1097–1106.
Robbrecht, E., D. Berghmans, and R. A. M. Van der Linden (2006), Objective CME detection over the solar cycle: A first attempt, *Adv. Space Res.*, *38*, 475–479.
Schmidt, J. M., and P. J. Cargill (2001), Magnetic cloud evolution in a two-speed solar wind, *J. Geophys. Res.*, *106*(A5), 8283–8289.
Simnett, G. M. (2005), CMEs observed by SMEI which are not seen by LASCO, *Solar Wind Eleven*, edited by B. Fleck and T. H. Zurbuchen, *Eur. Space Agency Spec. Publ., ESA SP-592*, 767–770.
Smith, Z., D. Odstrcil, and M. Dryer (1998), A 2.5-dimensional MHD parametric study of interplanetary shock interactions with the heliospheric current sheet/heliospheric plasma sheet, *J. Geophys. Res.*, *103*(A9), 20,581–20,589.
St. Cyr, O. C., et al. (2000), Properties of coronal mass ejections: SOHO LASCO observations from January 1996 to June 1998, *J. Geophys. Res.*, *105*(A8), 18,169–18,185.
Steinolfson, R. S. (1992), Coronal shock waves, in *Study of the Solar-Terrestrial System*, edited by J. J. Hunt, *Eur. Space Agency Spec. Publ, ESA SP-346*, 51–57.
Subramanian, P., K. P. Dere, N. B. Rich, and R. A. Howard (1999), The relationship of coronal mass ejections to streamers, *J. Geophys. Res.*, *104*(A10), 22,321–22,330.
Tappin, S. J. (2006), The deceleration of an interplanetary transient from the Sun to 5 AU, *Sol. Phys.*, *233*, 233–248.
Tappin, S. J., et al. (2004), Tracking a major interplanetary disturbance with SMEI, *Geophys. Res. Lett.*, *31*, L02802, doi:10.1029/2003GL018766.
Tokumaru, M., M. Kojima, K. Fujiki, and A. Yokobe (2000), Three-dimensional propagation of interplanetary disturbances detected with radio scintillation measurements at 327 MHz, *J. Geophys. Res.*, *105*(A5), 10,435–10,453.
Vourlidas, A., and R. A. Howard (2006), The proper treatment of coronal mass ejection brightness: a new methodology and implications for observations, *Astrophys. J.*, *642*, 1216–1221.
Vourlidas, A., S. T. Wu, A. H. Wang, P. Subramanian, and R. A. Howard (2003), Direct detection of a coronal mass ejection-associated shock in large angle and spectrometric coronagraph experiment white-light images, *Astrophys. J.*, *598*, 1392–1402.
Wang, Y.-M., and N. R. Sheeley Jr. (2006), Observations of flux rope formation in the outer corona, *Astrophys. J.*, *650*, 1172–1183.
Webb, D. F., and E. W. Cliver (1995), Evidence for magnetic disconnection of mass ejections in the corona, *J. Geophys. Res.*, *100*(A4), 5853–5870.
Webb, D. F., J. Burkepile, T. G. Forbes, and P. Riley (2003), Observational evidence of new current sheets trailing coronal mass ejections, *J. Geophys. Res.*, *108*(A12), 1440, doi:10.1029/2003JA009923.
Webb, D. F., et al. (2006), Solar Mass Ejection Imager (SMEI) observations of coronal mass ejections (CMEs) in the heliosphere, *J. Geophys. Res.*, *111*, A12101, doi:10.1029/2006JA011655.
Xue, X. H., C. B. Wang, and X. K. Dou (2005), An ice-cream cone model for coronal mass ejections, *J. Geophys. Res.*, *110*, A08103, doi:10.1029/2004JA010698.
Yashiro, S., N. Gopalswamy, G. Michalek, O. C. St. Cyr, S. P. Plunkett, N. B. Rich, and R. A. Howard (2004), A catalog of white light coronal mass ejections observed by the SOHO spacecraft, *J. Geophys. Res.*, *109*, A07105, doi:10.1029/2003JA010282.
Zhao, X. P., J. T. Hoeksema, Y. Liu, and P. H. Scherrer (2006), Success rate of predicting the heliospheric magnetic field polarity with Michelson Doppler Imager (MDI) synoptic charts, *J. Geophys. Res.*, *111*, A10108, doi:10.1029/2005JA011576.

S. W. Kahler, Air Force Research Laboratory/VSBXS, 29 Randolph Road, Hanscom AFB, MA 01731-3010, USA. (stephen.kahler@hanscom.af.mil)

D. F. Webb, Institute for Scientific Research, Boston College, Chestnut Hill, MA 02467, USA.